Study of the internal flow field in a pump-as-turbine (PaT): Numerical investigation, overall performance prediction model and velocity vector analysis

Study of the internal flow field in a Pump-as-Turbine (PaT): numerical investigation, overall performance prediction model and velocity vector analysis

David Štefan[1]

Viktor Kaplan Department of Fluid Engineering, Faculty of Mechanical Engineering, Brno University of Technology, Technická 2896/2, 616 69 Brno, Czech Republic

Mosè Rossi

Faculty of Science and Technology, Free University of Bozen/Bolzano, Piazza Università 5, 39100 Bolzano, Italy

Martin Hudec

Viktor Kaplan Department of Fluid Engineering, Faculty of Mechanical Engineering, Brno University of Technology, Technická 2896/2, 616 69 Brno, Czech Republic

Pavel Rudolf

Viktor Kaplan Department of Fluid Engineering, Faculty of Mechanical Engineering, Brno University of Technology, Technická 2896/2, 616 69 Brno, Czech Republic

Alessandra Nigro, Massimiliano Renzi

Faculty of Science and Technology, Free University of Bozen/Bolzano, Piazza Università 5, 39100 Bolzano, Italy

Abstract

This work presents a detailed analysis of the three-dimensional flows in a Pump-as-Turbine (PaT). The flow field is studied through URANS simulations and a velocity vector analysis. Moreover, a prediction model is used to forecast the performance of the PaT. The results of these methodologies were validated using experimental results. Flow rate and head at Best Efficiency Point (BEP) in turbine mode were 27% and 41% higher than the ones in pump mode, respectively; the mechanical efficiency was 4% lower. To give a fluid flow interpretation of this behaviour, velocity triangles in turbine mode were analytically calculated, as well as numerically evaluated. The analytically identified PaT flow rate at BEP is in agreement with CFD and measurements. Only small differences

Email address: `stefan@fme.vutbr.cz` (David Štefan)
[1]Corresponding author

appear, which might be explained by three reasons: i) the real flow angle is influenced by the finite number of blades and their thickness, ii) the PaT leading edge has a sharp ending since the impeller is designed to operate only in pump mode and iii) tapering of the meridional cross-section from volute to impeller. While close to the BEP the mechanical efficiency is flat, a sensible drop caused by flow detachments and swirling flows was detected at part-load.

Keywords: Pump-as-Turbine, Unsteady CFD simulations, Experimental data, Performance prediction model, Velocity triangles.

1. Introduction

The energy production from renewable resources, aimed at reducing the green-house gas emissions, is recognized worldwide as a priority. In the last decades, the research on this field is showing a great progress and the technologies developed to exploit clean energy sources are becoming more and more attractive. Among them, hydropower is one of the most traditional and widespread: indeed, several investigations have been conducted on both large and small scale plants as well as in Water Distribution Networks (WDNs) through energy recovery interventions [1, 2, 3].

Regarding the mini- and micro-scale plants, Pump-as-Turbine (PaT) technology is one of the emerging solutions due to several reasons: i) it is cheaper than a traditional hydraulic turbine, ii) it relies on a massive production of pumps together with a wide choice of sizes and solutions and iii) there is a high availability of spare parts in the market [4, 5, 6]. Because of this, the research on both performance and design of PaTs is increasing and becoming of large interest.

One of the biggest issues for the choice of the proper machine to be used in a given application is the lack of performance data of pump operating in turbine mode. Literature is rich of models and methodologies that are used to predict the Best Efficient Point (BEP) of a PaT using the corresponding operative parameters in pump mode [7, 8, 9]. It is worth noticing that new models are still being developed and studied, such as in [10, 11]. These models are also complemented with other solutions like 1D numerical codes [12], theoretical approaches [13, 14], analytical methods [15], Hermite polynomials expressions [16] and physics-based models [17] to forecast the global performance of PaTs when operating in off-design conditions. Only recently, researchers involved in the study of the PaTs performance forecast have been able to collect more experimental data to use in the development of their respective models, such as [15, 16], in order to widen their range of applicability. Among them, some of the authors of this work [18] developed an analytical model, based on a statistical analysis of experimental data related to 32 different PaTs, capable of forecasting the off-design operating conditions in turbine mode knowing the BEP of the PaT running in reverse mode. This methodology is based on using the non-dimensional parameters and the normalization process with respect to the PaT BEP magnitudes in turbine mode.

Besides the aforementioned models, several other approaches based on experimental and Computational Fluid Dynamics (CFD) analyses [19, 20, 21] were performed in order to suggest possible design improvements of PaTs operating in turbine mode, aimed at increasing the overall performance. After the validation of the CFD simulations with the experimental results, the numerical analysis has been widely used so far for the prediction of the hydraulic machines performance by inspecting their operating points and the flow phenomena that could occur inside them [22, 23, 24]. The performance forecast provided by the CFD simulations can be more accurate than the ones obtained through the analytical/theoretical models, even though their applicability is strongly dependent on the analysed machine, as well as being time demanding due to the definition of a proper numerical set-up. Regarding these aspects, easy analytical/theoretical correlations obtained using experimental data allow machines users to predict quickly their performance according to the specific speeds or specific diameters ranges of the pumps/turbines with which the model has been developed. On the PaT point of view, most of these studies focused the attention on their operation at BEP in steady-state conditions [25, 26]. Nevertheless, the employed steady-state CFD simulations often lead only to a partial understanding of the problem that may occur when the pump is operating in turbine mode, especially far from its BEP. Only recently, due to the increase of computational power and the development of numerical models, some researchers have started to investigate the complex unsteady fluid dynamics phenomena that occur inside PaTs operating in off-design conditions by the means of Unsteady Reynolds Averaged Navier-Stokes (URANS) equations [27, 28]. Su et al. [29] numerically investigated the internal flow behaviour of three PaTs, having different specific speeds, in order to analyse the periodic phenomena that occur in the rotor-stator gaps. Since transient simulations were performed, the time dependent flow rate was captured and analysed in the computational fluid domains on both Lagrangian and Eulerian points of view. Furthermore, the numerical results for three PaTs were validated through laboratory tests. Yang et al. [30] studied the dynamics of unsteady flows in a multistage pump-turbine, focusing the attention on the first stage. Both experimental tests and numerical simulations, using the Detached Eddy Simulation (DES) model, were employed to deeply study the internal flow field, revealing the presence of specific flow patterns. Barrio et al. [31] performed a numerical investigation on the unsteady flow in a commercial centrifugal pump operating in both direct and reverse mode with the help of CFD codes. The results of the simulations were in accordance with the experimental ones, revealing that in reverse mode operation the flow matched the geometry of the impeller only at rated operating conditions. On the contrary, re-circulating fluid regions are created near the Trailing Edge (TE) of the blades at part-load conditions and close to the Leading Edge (LE) at high flow rates.

In this work, experimental data of a PaT operating in both pump and turbine modes are presented; a validation of both CFD simulations and performance prediction model was performed by using the experimental results obtained in turbine mode. The purpose of this study is twofold: i) to validate both numerical and prediction models for the forecast of PaTs performance developed by some of the authors of this work [18] by means of the experimental results in turbine mode; ii) to better understand the fluid behaviour inside a commercial centrifugal pump operating in turbine mode, focusing the attention on the flow instabilities that take place when it operates at very low part-load conditions. To this end, unsteady numerical simulations were performed with the commercial CFD solver ANSYS® CFX by investigating the tested flow rates. In particular, the flow instabilities generated in the PaT were assessed by analysing the velocity triangles at the volute-impeller and impeller-discharge pipe interfaces obtained with the CFD simulations and with analytical calculations. A theoretical evaluation was carried out in the locations previously mentioned by considering both an infinite and a finite blade count of the impeller. Subsequently, the obtained results were compared with the numerical ones, showing a quite good accordance on detecting the BEP flow rate evaluated considering the finite blade count. Finally, it was thoroughly demonstrated how the finite blade count affects the analytic evaluation of the velocity components. The streamlines that are present in the volute, impeller and discharge pipe are shown by different view angles in order to further investigate which kinds of instabilities occur.

The paper is structured as follows: Section 2 describes the most important characteristics of the PaT and the experimental apparatus employed to obtain its global performance when operating in turbine mode together with the used equipment. In Section 3, the numerical modelling, including the grid independence study, is presented. Furthermore, Section 4 briefly describes the prediction model for PaTs performance forecast that was developed by some of the authors of this work [18]. Section 5 is devoted to the validation of the URANS CFD results, as well as the ones predicted by the model of [18], through the experimental ones when the PaT operates in turbine mode. After this, the fluid dynamic behaviour and the flow instabilities in the hydraulic machine were investigated by deeply inspecting the values of the velocity triangles, obtained on both theoretically and numerically points of view, at the volute-impeller and impeller-discharge pipe interfaces when the PaT operates in turbine mode. Finally, Section 6 reports the conclusions of the work.

2. Experimental set-up

The experimental tests were performed on a centrifugal pump operating in both direct (pump) and reverse (turbine) modes. The characteristics of the machine and of the liquid used in tests are summarized in Table 1. It is worth noticing that the specific speed has been evaluated using Eq. (1).

$$N_S = \omega \cdot \frac{\sqrt{Q}}{\sqrt[4]{(g \cdot H)^3}} \tag{1}$$

Figure 1 reports the Process Flow Diagram (PFD) of the test-rig where the dotted blue lines refer to the layout of the PaT testing in pump mode (Pump), while the continuous ones refer to the PaT testing in turbine mode (Pump-as-Turbine). A flow meter, indicated as FI in Figure 1, was used to measure the

Table 1: Main parameters of the tested centrifugal pump

Rotational speed [rpm]	2900
Impeller outer diameter [m]	0.174
Specific speed	0.69
Impeller blade count	6
Suction pipe diameter [m]	0.1
Volute outlet pipe diameter [m]	0.064
Exploited liquid	H_2O @ 25°C and 1 bar

volumetric flow rate (Q) elaborated by the hydraulic machine in both operating modes and it was located far from the discharge of the PaT running in pump mode.

Eight pressure probes, indicated as PI in Figure 1, were equally distributed along the circumferential direction of the pipes and placed upstream and downstream the hydraulic machine in order to evaluate the delivered head (H). Specifically, considering the PaT operating in pump mode, four probes were located in the inlet pipe at 0.40 m from the corresponding opening, which represents a distance equal to four times the diameter of the inlet pipe. Other four probes were placed in the discharge pipe at 0.45 m from the respective opening, equivalent to a distance of seven times the diameter of the corresponding discharge opening. The same distances were kept fixed also when the PaT was tested in turbine mode.

The mechanical torque (T) transmitted by the motor to the pump shaft is measured by a torque sensor located on the shaft between the PaT and the electric motor/generator. Both pump and turbine modes were measured at constant rotational speed. The flow rate exploited by the centrifugal hydraulic machine in turbine mode was ensured by the supply pump, whose motor was controlled through a frequency converter.

The laboratory equipment and their main characteristics are listed in Table 2, while the average uncertainties of the measured (Q, T) and derived (H, η) quantities are reported in Table 3.

Table 2: Laboratory equipment and their main characteristics

Type of instrument	Manufacturer	Measurement range	Accuracy
Flow meter	Krohne	$2 - 40$ l/s	$\pm 2\%$
Pressure probe	BD	4 bar	$\pm 0.25\%$
Torque meter	Kistler Staiger Mohilo	100 Nm	Class 0.2
Dynamometer	TES Vsetín	22.4 kW	-

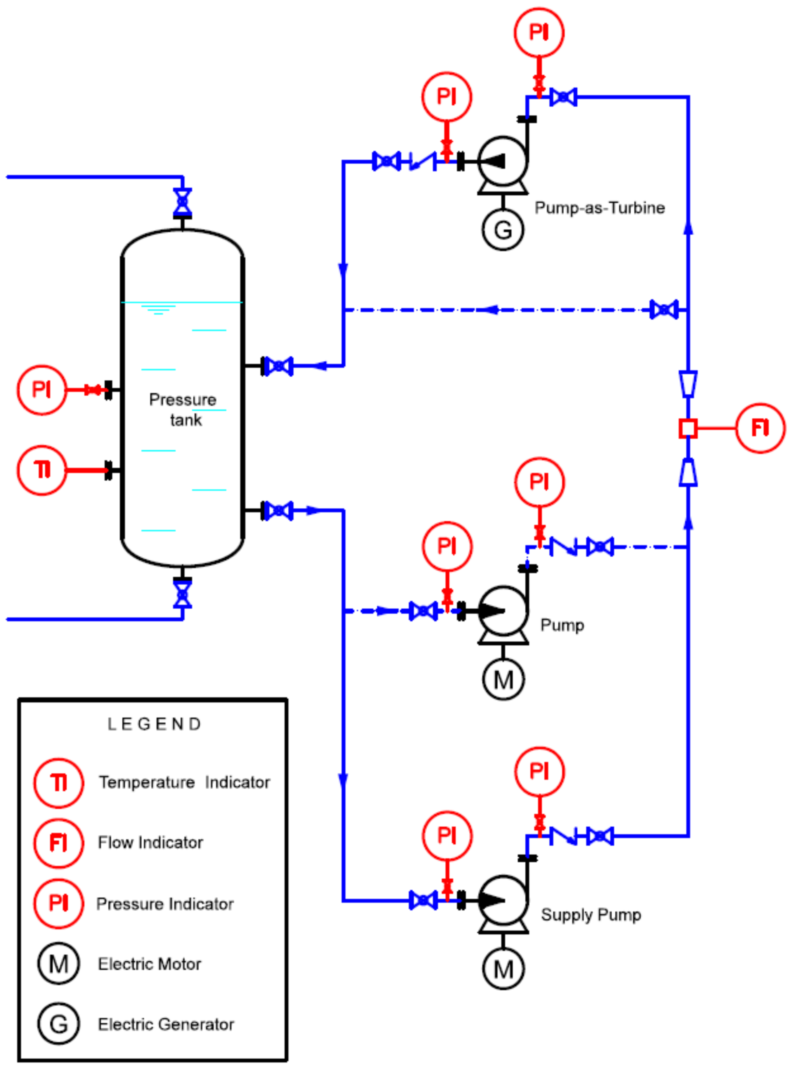

Figure 1: Process Flow Diagram (PFD) of the used test rig

Table 3: Uncertainty of the measured and derived quantities

Magnitude	Uncertainty
Volumetric flow rate (Q) [l/s]	0.56
Head (H) [m]	0.16
Efficiency (η)	1%
Torque (T) [Nm]	0.2

The experimental tests of the centrifugal pump operating in both pump and turbine modes consisted in the acquisition of the relevant performance data of 11 and 8 different operating conditions, respectively, BEP included. These data were evaluated by varying the volumetric flow rate: Table 4 reports the tested flow rates, which are sorted in ascending order from left to right, in both pump and turbine operating modes, respectively. For sense of clarity, the values recorded at the BEP are in bold.

Table 4: Volumetric flow rates exploited in both pump mode and in turbine modes

Pump $\left[\frac{m^3}{s}\right]$	0.000	0.0031	0.0099	0.0134	0.0171	0.0224	0.0263	0.0304	**0.0323**	0.0368	0.0400
Turbine $\left[\frac{m^3}{s}\right]$	0.0175	0.0219	0.0261	0.0312	0.0360	0.0391	**0.0409**	0.0415	–	–	–

3. Numerical modelling

The numerical simulations were performed by means of the commercial CFD software ANSYS® CFX, which is based on the Finite Volume Method. URANS simulations were applied on the 3D model of the tested centrifugal PaT, operating in both direct and reverse modes, using the steady-state flow field as initial condition. Details of the computational domain and of the Boundary Conditions (BCs) to perform the URANS simulations are discussed together with a mesh independence study that was carried out by successive refinements of the overall computational grid. Finally, the numerical set-up and the discretization schemes employed to compute the flow field in both direct and reverse modes are analysed.

3.1. Computational domain and BCs

The computational domain is divided in four sub-volumes: inlet pipe, volute, impeller and discharge pipe as shown in Figure 2. It is worth noticing that the sub-volumes named inlet pipe and discharge pipe, which are displayed in Figure 2, refer to the hydraulic machine when it operates in turbine mode.

The sub-volumes are created to simplify the meshing process and, above all, to consider the relative rotation of the impeller with respect to both volute and pipes. Both inlet and discharge pipes are added to fix the BCs as uniform physical quantities in the inlet and the discharge sections, respectively, without affecting the results of the simulations. For this purpose, a length equal to 10 times the respective diameters of the volute openings are added in the intake and discharge sections and linked to the volute. This allows to have a fully developed flow and to avoid reverse flows in proximity of the volute opening at the discharge, thus affecting the reliability of the numerical results.

It is worth noticing that the computational domain used for the CFD analysis is an approximation of the real tested hydraulic machine since the 3D model of the impeller was reconstructed ex-novo and matched with the 3D model of the volute.

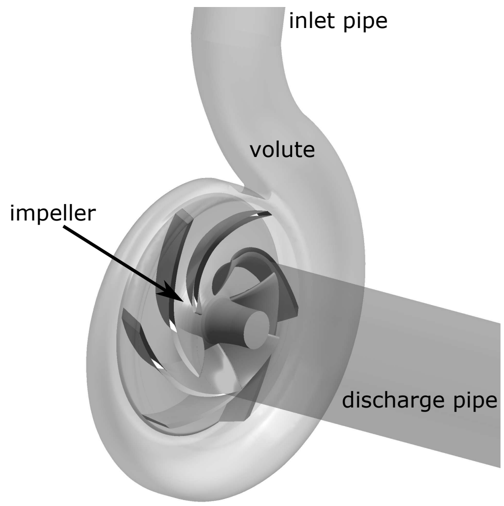

Figure 2: Overall computational fluid domain

As regards the leakage flows, no impeller clearance have been considered: therefore, the numerical results do not take into account the volumetric losses due to the leakages passing through the gaps between the impeller and the volute casing. In a same way, the drag friction losses in the back of the impeller disks are neglected in the numerical results. Furthermore, the numerical analysis does not consider also the mechanical friction losses due to the rotation of the shaft and of the bearings.

In order to consider these effects, the hydraulic efficiency obtained by the CFD simulations $\eta_{h(CFD)}$ was further corrected before comparing it with the experimental results. Both leakage flow and disk friction losses were estimated using the methodology presented by Gulich [32]. By knowing the geometry of the impeller side wall gaps and the annular seal, the leakage flow Q_v was calculated resulting in an average value $Q_v = 6.12 \cdot 10^{-4}$ m^3/s when the PaT operates in turbine mode. From this, the volumetric efficiency is calculated as follows $\eta_v = \frac{Q-Q_v}{Q}$, with an average value $\eta_v = 0.98$. The power loss due to disk friction at rated PaT operational speed $n = 2900$ rpm was estimated to be $P_d = 892$ W, which is around 5 % of the PaT hydraulic power at BEP. Consequently, the disk friction losses are integrated into the equation for the evaluation of the hydraulic efficiency as follows.

$$\eta_h = \frac{2\pi n T - P_d}{\rho Q g H} \tag{2}$$

The mechanical efficiency η_m was considered equal to $\eta_m = 0.95$ and constant for all the operating points. This value was found to be adequate for both geometrical assembly and age of the investigated machine. Finally, the overall efficiency is estimated as follows

$$\eta = \eta_h \cdot \eta_v \cdot \eta_m. \tag{3}$$

The BCs adopted for the simulations in turbine mode are reported in Table 5. The turbulence intensity in correspondence of the inlet section is unknown but, since the inlet BC is positioned far away from upstream disturbances, it was assumed a low turbulence intensity $I = 5\%$ that is defined as the ratio between the Root Mean Square (RMS) of the velocity fluctuations and the mean flow velocity.

As regards the other BCs, nine experimental values of volumetric flow rates (Q) at the inlet section of the hydraulic machine have been used as listed in Table 4. Finally, an average static pressure equal to 1 bar was imposed at the discharge section.

Table 5: BCs of the CFD simulations of the PaT operating in turbine mode

Boundary	Boundary conditions	Imposed values
Inlet	Volumetric flow rate	$Q = (0.018 - 0.059)$ $[m^3/s]$
	Turbulence intensity	$I = 5\%$
Outlet	Average static pressure	1 [bar]
Walls	No-slip conditions	$\mathbf{v}$ relative to the boundary= 0
	Adiabatic wall	Normal heat flux= 0

3.2. Computational grid and convergence study

The mesh of the impeller channels was generated by means of ANSYS® TurboGrid, while the meshes of both volute and pipes were created with the ANSYS® Mesh tool.

In order to carry out the grid independence study, which is intended to asses if the mesh size affects the results, unsteady simulations of three different grids were performed at BEP of the PaT operating in turbine mode and the obtained numerical results have been compared. The grid sizes were changed gradually taking into account each computational sub-domain. Table 6 summarizes the number of elements, in particular the sub-domains regarding coarse (G3), medium (G2) and fine (G1) grids. Three main physical magnitudes have been considered: head (H), torque (T) and hydraulic efficiency (η_h).

Table 6: Grids sizes of particular domains

Grid	Inlet Pipe	Impeller	Volute	Discharge Pipe	Σ of elements
G1	$1,585,963$	$15,686,784$	$585,554$	$365,292$	$18,223,593$
G2	$1,130,676$	$12,029,184$	$446,198$	$265,321$	$13,871,379$
G3	$796,300$	$8,994,888$	$434,021$	$206,405$	$10,431,614$

In this work, the Grid Convergence Index (GCI) method that was introduced by Roache et al. [33, 34] was used to evaluate the grid convergence. The method described by Celik [35] is defined as follows: the average grid size G of the cell in the fluid domain is evaluated using Eq. (4)

$$G = \left[\frac{1}{N} \sum_{i=1}^{N} (\Delta V_i) \right]^{\frac{1}{3}}, \tag{4}$$

where ΔV_i is the i-th element's volume and N is the total number of elements. Head, torque and efficiency were considered as variables ϕ for the estimation of the GCI in order to verify the mesh independence. The grid refinement factor (r) was computed as $r = G_{fine}/G_{coarse}$; thus, for $G_1 < G_2 < G_3$, it follows that $r_{21} = G_2/G_1$ and $r_{32} = G_3/G_2$. Subsequently, the extrapolated values are calculated according to Eq. (5) where p is the apparent order of the method.

$$\phi_{ext}^{21} = \left[\frac{r_{21}^p \phi_1 - \phi_2}{r_{21}^p - 1} \right] \tag{5}$$

Approximate relative errors are calculated by means of Eq. (6) and the extrapolated relative error was estimated using Eq. (7).

$$e_a^{21} = \left[\frac{\phi_1 - \phi_2}{\phi_1} \right] \tag{6}$$

$$e_{ext}^{21} = \left[\frac{\phi_{ext}^{21} - \phi_2}{\phi_{ext}^{21}} \right] \tag{7}$$

Finally, the GCI index, which is obtained with the "fine to medium grid", is evaluated with Eq. (8)

$$GCI_{fine}^{21} = \left[\frac{1.25 e_a^{21}}{r_{21}^p - 1} \right] \tag{8}$$

The different evaluated GCI indexes are summarized in Table 7.

Table 7: GCI indexes for head, torque and hydraulic efficiency values

	H [m]	T [Nm]	η_h [-]
GCI_{fine}^{21}	$2.27 \cdot 10^{-4}$	$4.85 \cdot 10^{-4}$	$2.27 \cdot 10^{-4}$
GCI_{med}^{32}	$9.75 \cdot 10^{-6}$	$5.30 \cdot 10^{-5}$	$3.51 \cdot 10^{-5}$

Since all the three grids are sufficiently large (even the coarse grid with 10.5 M elements), both GCI indexes GCI_{fine}^{21} and GCI_{med}^{32} are very small for all the three tested quantities of delivered head H, torque T and hydraulic efficiency η_h. This analysis indicates that each tested computational sub-domain resolution leads to mesh independent results considering the chosen numerical set-up. Nevertheless, the finer grids of each computational sub-domain were used in all the CFD simulations presented in this study in order to have a safety margin with respect to other more demanding operating conditions.

Figure 3 shows two images of the spatial discretization used to solve the flow equations: a global view is presented in Figure 3a, while Figure 3b shows the structured grid of impeller domain.

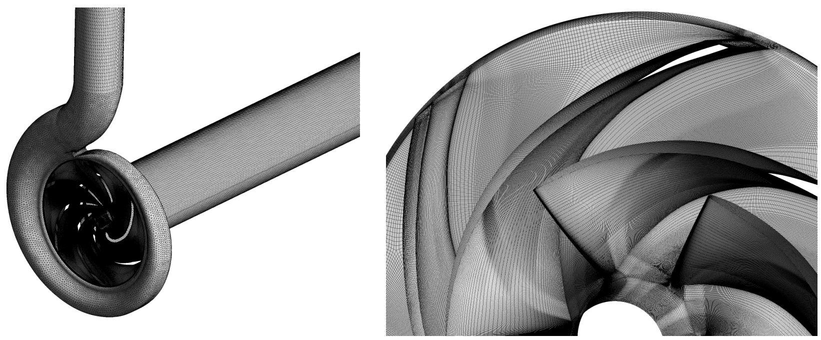

(a) Global view (b) Detail of the impeller domain

Figure 3: Computational grid

3.3. Turbulence model and numerical schemes

In this paper, unsteady CFD simulations are performed on a PaT operating in turbine mode solving the URANS equations augmented with the standard $k-\epsilon$ turbulence two-equations model with a scalable wall function.

It is worth noticing that steady-state simulations, using the Reynolds Averaged Navier-Stokes (RANS) equations, were also run preliminary to get the initial flow fields and to speed up the convergence of the unsteady ones.

The $k-\epsilon$ model is robust and fast to accurately calculate the majority of the industrial problems, including also hydraulic pumps and turbines. As shown in [36, 37, 38, 39, 40] the $k-\epsilon$ model provides a good prediction of the fluid flow inside hydraulic machines considering different operating conditions and it also well predicts strong swirling flows [41, 42]. However, its limitation can be found when isotropic turbulent viscosity assumption is made: in other words, the ratio between the Reynolds stress and the mean rate of deformation is the same in all directions, leading to inaccurate solutions for large curvature flows and flows that tend to separate. On the other hand, the $k-\epsilon$ model allows to run numerical calculations on grids where the wall function approach can be used, including also the ones where the non-dimensional wall distance $y^+ = u_* y/\nu$ ranges between 30 and 300 [43], [44]. Moreover, the scalable wall function relaxes the requirement on the height of the first wall element by means of a wall model formulation based on y^* with an automatic cut-off value. The $k-\epsilon$ model was chosen in this study due to its numerical robustness that leads to converged solutions in relatively short time compared to other turbulence modeling approaches such as Reynolds Stress Model (RSM) or Detached Eddy Simulation (DES).

The change of reference frame from stationary to rotating and vice-versa was performed with the "Transient Rotor-Stator Interface" [30, 45] that allows to exchange the information of both velocity and pressure with the appropriate relative velocity obtained in the two domains of interest, which are the rotor and the stator.

To reduce the numerical diffusion, the "High-Resolution" option was selected for both advection scheme and turbulence numeric.

The Second Order Backward Euler scheme was used to discretize the time dependent terms of the governing equations and five inner iteration loops were considered in one time step with size of $\Delta t = 1.724 \cdot 10^{-4}s$, corresponding to 3° of a rotor rotation angle [31, 29].

The convergence was checked by monitoring the variation of the RMS residuals between successive iterations. The calculation process was stopped when a very low percentage variation was reached. The normalized residuals drop, considering all the performed simulations, was between 10^{-5} and 10^{-6}.

Finally, y^+ values in each sub-domain were checked and the following results were obtained: $y^+ = 72$ at the impeller blades, $y^+ = 111$ at the shroud, $y^+ = 81$ at the hub, $y^+ = 143$ at the volute, $y^+ = 90$ at the inlet pipe and $y^+ = +52$ at the discharge pipe, respectively. All the y^+ values are within 30 and 300, which is the range suggested by the software guidelines when analyzing this kind of problem [46].

4. PaT prediction model

The analytical model developed by [18] is used to supply a figure of the PaT performance in reverse mode. The model requires the operating data of the PaT at BEP in turbine mode as input and allows to reconstruct its performance curves when running in turbine mode [47]. In this work the forecast capability of the model is assessed by comparing the output of the calculations with the experimental results in turbine mode. The outcomes of the CFD simulations are also used in order to give a punctual explanation of the forecasts of the model. The presented model is based on the experimental data related to the performance of 32 PaTs. A non-dimensional analysis is carried out in order to obtain the flow coefficient (φ) and the head coefficient (ψ) per each PaT included in the data-set. Furthermore, the non-dimensional coefficients were normalized with respect to their corresponding values at BEP in turbine mode.

For sense of clarity, Eqs. (9) and (10) report the definitions of both flow coefficient (φ) and the head coefficient (ψ), respectively, where g, ω and D are the gravity acceleration [m/s^2], rotational speed [rad/s] and the outer impeller diameter [m], respectively. The efficiency is already a non-dimensional value since it is obtained by the ratio between the mechanical power, which is obtained multiplying the measured torque with the rotational speed, and the hydraulic one. This statement is valid when the PaT operates in turbine mode, while it is reversed when the PaT operates in pump mode.

$$\varphi = \frac{Q[m^3/s]}{\omega[rad/s] \cdot D^3[m^3]} \tag{9}$$

$$\psi = \frac{g[m/s^2] \cdot H[m]}{\omega^2[rad^2/s^2] \cdot D^2[m^2]} \tag{10}$$

Results showed that the operating points of the PaTs, after the normalization process, are laying on a single trend independently of the size and typology of machine. Therefore, the performance curves were built by interpolating the non-dimensional and normalized experimental data-set by means of polynomial equations. Specifically, both non-dimensional characteristic and efficiency curves were obtained with a good accuracy: regarding the first curve, the R^2 value was equal to 0.9171, while for the second one it was equal to 0.7856. This latter value is lower than the previous one and this outcome is due to the higher dispersion of some experimental data in correspondence of flow rates much lower than the BEP. In fact, at part-load conditions, the design characteristics of the PaTs (type of the impeller, number of blades, size of the clearance, etc.) can affect their behaviour and determine detachment phenomena that are hard to be predicted and vary from one PaT design to another. However, it is suggested to use this prediction model in the range ±40% of flow rates with respect to the BEP one. The non-dimensional and normalized characteristic and efficiency curves of the predicting model are shown in Figures 4 and 5 along with their analytical description through Eq.s (11) and (12), respectively.

$$\psi/\psi_{BEP} = 0.2394\left(\varphi/\varphi_{BEP}\right)^2 + 0.769\left(\varphi/\varphi_{BEP}\right) \tag{11}$$

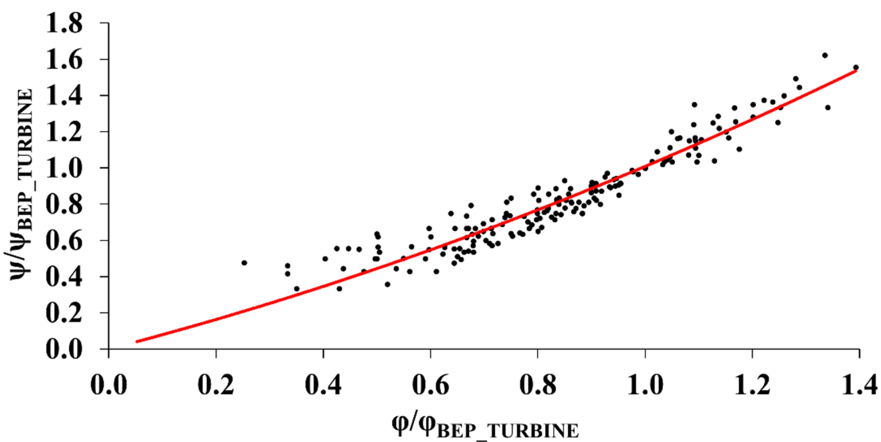

Figure 4: Non-dimensional characteristic curve [18]

$$
\begin{aligned}
\eta/\eta_{BEP} = & -1.9788\left(\varphi/\varphi_{BEP}\right)^6 + 9.0636\left(\varphi/\varphi_{BEP}\right)^5 \\
& -13.148\left(\varphi/\varphi_{BEP}\right)^4 + 3.8527\left(\varphi/\varphi_{BEP}\right)^3 \\
& +4.5614\left(\varphi/\varphi_{BEP}\right)^2 - 1.3769\left(\varphi/\varphi_{BEP}\right)
\end{aligned} \tag{12}
$$

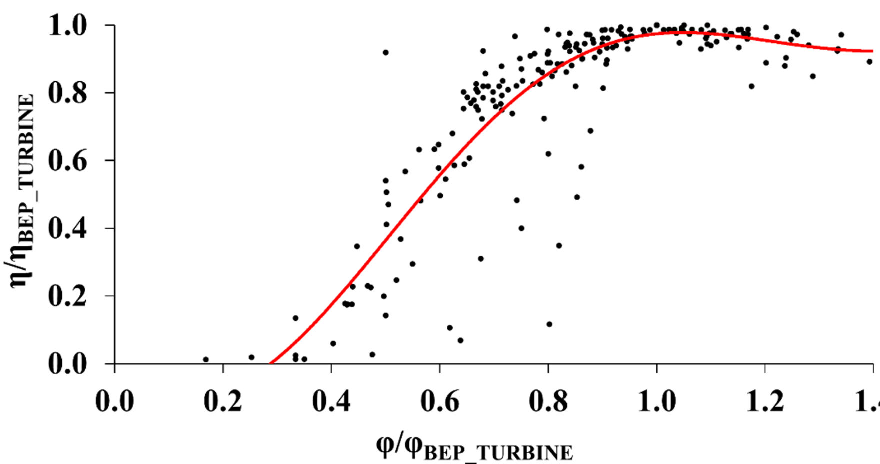

Figure 5: Efficiency curve [18]

Here in after, the non-dimensional and normalized quantities named $\varphi_n = \varphi/\varphi_{BEP}$, $\psi_n = \psi/\psi_{BEP}$, $\eta_n = \eta/\eta_{BEP}$ will be used to study the performance of the analysed PaT.

5. Results & Comments

Comparing the BEP values obtained experimentally in both pump and turbine modes (see Table 4), it was noticed that the BEP flow rate increases in turbine mode, being in accordance with the literature: indeed, most of the works involved in the study of the PaTs assess that these hydraulic machines, operating at their BEP, exploit a higher flow rate with respect to the one in pump mode [48]. The same behaviour is generally recorded also for the head value. Regarding the efficiency, some PaTs achieve a value in turbine mode that is not different to the one in pump mode, meaning that it could be slightly lower, equal or higher depending on the PaT typology [49]. Precisely, in this case $\varphi_{BEP_{TURBINE}} = 1.27 \cdot \varphi_{BEP_{PUMP}}$, $\psi_{BEP_{TURBINE}} = 1.41 \cdot \psi_{BEP_{PUMP}}$ and $\eta_{BEP_{TURBINE}} = 0.96 \cdot \eta_{BEP_{PUMP}}$ have been reached.

In this Section, the values obtained from the numerical simulations are presented in turbine mode taking into account the correction factors due to disk friction losses and both volumetric and mechanical efficiencies of the PaT. The results are subsequently compared with the experimental ones and validated. After the validation of the CFD simulations, the attention is focused on the study of the PaT internal fluid flow behaviour and on the comparison with the aforementioned model.

Thanks to the detailed analysis of the PaT, it was possible to analyse the velocity triangles and the fluid flow phenomena inside the hydraulic machine in turbine mode. In particular, a theoretical evaluation of the velocity triangles, by assuming both finite and infinite blade count of the impeller, is performed and the obtained values are compared with the numerical ones. Moreover, the internal fluid behaviour was also studied to assess the different efficiency trends when the PaT operates at part-load operating conditions.

Before starting the discussion and the analysis of the PaT behaviour in turbine mode, Figure 6 shows the experimental non-dimensional performance curves of the PaT operating in pump mode, related to the characteristic curve (a) and the mechanical efficiency one (b), respectively. The BEP conditions are highlighted by red plus sign (+). In addition, Table 8 lists the non-dimensional values plotted in Figure 6.

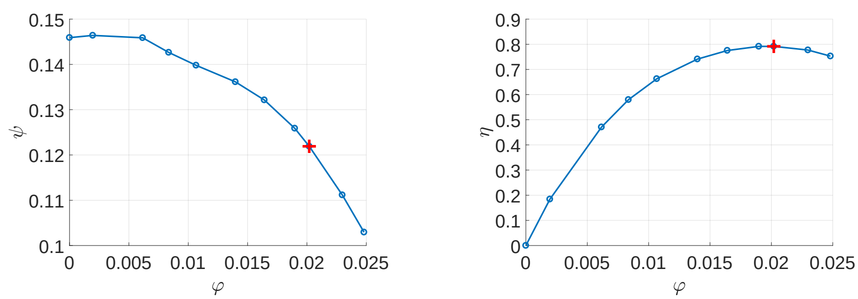

(a) Non-dimensional characteristic curve

(b) Mechanical efficiency curve

Figure 6: Experimental results of pump mode operation in terms of (a) characteristic and (b) mechanical efficiency curves

Table 8: Experimental data of the PaT operating in pump mode

φ	ψ	η
0.0000	0.1459	0.000
0.0020	0.1464	0.184
0.0062	0.1459	0.471
0.0084	0.1426	0.580
0.0107	0.1398	0.663
0.0140	0.1361	0.741
0.0164	0.1321	0.775
0.0190	0.1259	0.791
0.0202	**0.1219**	**0.792**
0.0230	0.1112	0.777
0.0248	0.1029	0.775

5.1. *Validation of the numerical model (turbine mode)*

The measured data, obtained through laboratory tests that were performed using the test bench described in the Section 2, were compared with the numerical ones for the validation process.

Figure 7 shows the comparison between the experimental and the numerical results of the PaT operating in turbine mode with BEPs highlighted by the red plus (+) and red cross (×) signs for experiment and CFD, respectively. Table 10 reports the obtained values together with the percentage relative differences, where the experimental results are taken as reference.

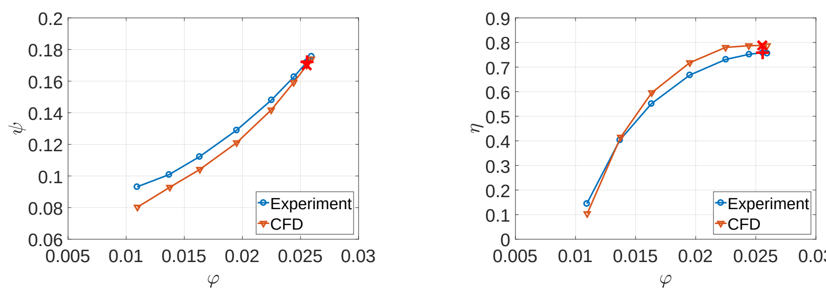

(a) Characteristic curve

(b) Mechanical efficiency curve

Figure 7: PaT operating in turbine mode: experimental vs CFD non-dimensional data in terms of (a) characteristic and (b) efficiency curves

The percentage relative difference of a generic variable a related to the numerical results is defined as:

$$\Delta a_{CFD}\% = \frac{(a_{Exp.} - a_{CFD})}{a_{Exp.}} \times 100 \tag{13}$$

In order to provide a complete analysis of the numerical validation, the non-dimensional experimental and numerical values of the PaT at BEP in turbine mode are reported in Table 9. Furthermore, all the non-dimensional values related to the inspected operating points, are listed in Table 10 together with the percentage relative differences as previously defined. It is worth noticing that there is a very small difference between the BEP flow rates obtained experimentally and numerically as Figure 7 shows. However, since the rounding of the flow coefficient magnitudes did not lead to significant variation of the numeric values, it can be assumed that the experimental flow rate at BEP matches with the numerical one.

Table 9: Non-dimensional values of the PaT at BEP in turbine mode (Exp. vs CFD)

	Exp.	CFD
φ	0.0255	0.0255
ψ	0.1722	0.1700
η	0.8587	0.7880

The results obtained with the CFD analysis are in accordance with the ones obtained in the experimental campaign as Figure 7 shows.

Also the values reported in Table 10 show that there is a general good agreement between CFD and experimental data.

In particular, the percentage relative differences of the operating points close to the BEP value, highlighted in bold in Table 10, are quite small, thus meaning that the CFD set-up was performed properly.

The highest absolute relative differences between experimental and numerical values are registered for the operating point of φ equal to 0.0109 regarding both head and efficiency, being close to 14% and 28%, respectively. This is mainly caused by the very low numeric value of the efficiency because even a small error could result in a very high relative difference.

It is very likely that the discrepancies between experimental and numerical results are mainly due to the simplification of the computational domain where the impeller sidewall gaps and leakage flow are not considered, even though, as described in Section 3.1, the relevant corrections for efficiency obtained from CFD were applied. Nonetheless, these corrections are based only on empirical equations which require hardly predictable values of impeller and volute surface roughness.

Table 10: PaT operating in turbine mode: experimental Vs numerical data

	Experimental		CFD		Relative differences %	
φ	ψ	η	ψ	η	$\Delta\psi\%$	$\Delta\eta\%$
0.0109	0.0913	0.1446	0.0803	0.1040	+13.80	28.06
0.0137	0.1009	0.4032	0.0929	0.4150	+7.94	−2.91
0.0163	0.1122	0.5511	0.1042	0.5960	+7.16	−8.15
0.0195	0.1290	0.6674	0.1210	0.7180	+6.20	−7.58
0.0225	0.1481	0.7312	0.1418	0.7800	+4.25	−6.67
0.0244	0.1628	0.7519	0.1592	0.7870	+2.22	−4.67
0.0255	**0.1722**	**0.7587**	**0.1700**	**0.7880**	**+1.27**	**−3.86**
0.0259	0.1757	0.7560	0.1740	0.7870	+0.96	−4.10

5.2. Comparison with the PaT prediction model

After the validation of the numerical model with the experimental results related to the PaT operating in turbine mode, the accuracy of the performance prediction model developed by [18] is assessed by using the same experimental data.

Figure 8 shows the comparison between the experimental and the predicted results of the PaT operating in turbine mode. Table 12 reports the obtained values together with the percentage relative differences, where the experimental results are taken as reference. In this case, the percentage relative difference

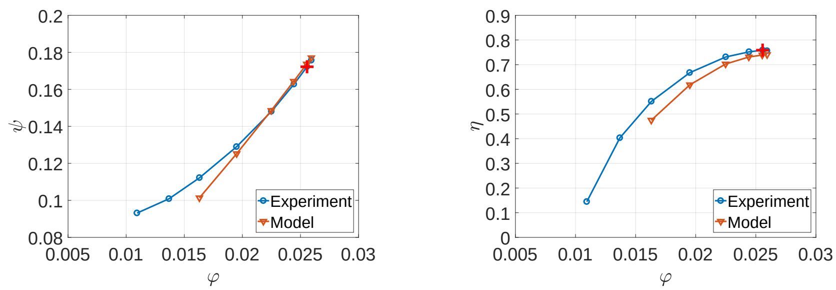

(a) Characteristic curve

(b) Mechanical efficiency curve

Figure 8: PaT operating in turbine mode: experimental vs predicted normalized data in terms of (a) characteristic and (b) mechanical efficiency curves

of a generic variable a related to the results of the used prediction model was defined as:

$$\Delta a_{mod.}\% = \frac{(a_{Exp.} - a_{mod.})}{a_{Exp.}} \times 100 \tag{14}$$

It is worth noticing that the normalized BEP values were not exactly equal to 1 as they are evaluated by using the characteristic and mechanical efficiency curves described by Eq. (11) and Eq. (12) where the passage to the point coordinates (1, 1) was not imposed.

For sake of completeness, considering that the flow coefficient at BEP was kept constant and equal to the experimental one, the non-dimensional predicted values at BEP in turbine mode are compared with the experimental ones as listed in Table 11.

In addition, Table 12 shows the comparison between non-dimensional predicted values and experimental ones when the PaT operates in off-design conditions, as well as the relative percentage differences previously defined.

Table 11: Non-dimensional values of the PaT at BEP in turbine mode (Exp.vs model)

	Exp.	Model
φ	0.0255	0.0255
ψ	0.1722	0.1736
η	0.8587	0.7406

Table 12: PaT operating in turbine mode: experimental Vs prediction model

	Experimental		Prediction model		Relative differences %	
φ	ψ	η	ψ	η	$\Delta\psi\%$	$\Delta\eta\%$
0.0163	0.1122	0.5511	0.1013	0.4748	+9.71	+13.85
0.0195	0.1290	0.6674	0.1252	0.6182	+2.95	+7.37
0.0225	0.1481	0.7312	0.1485	0.7025	−0.27	+3.93
0.0244	0.1628	0.7519	0.1643	0.7310	−0.92	+2.39
0.0255	**0.1722**	**0.7587**	**0.1736**	**0.7406**	**−0.82**	**+2.29**
0.0259	0.1757	0.7560	0.1770	0.7390	−0.74	+2.24

As concerns the comparison reported in Figure 8, there is a general good agreement between the values obtained by using the performance prediction model and the ones experimentally obtained, especially for operating points not so far from the BEP, while the differences between experimental and predicted values tend to increase going towards very low part-load operating conditions. Table 12 lists the relative percentage differences between the experimental and the model data. Results show that, when the PaT is operating with significantly lower flow rates than the one at BEP, the percentage relative differences increase, reaching an absolute maximum value of about 14%, in terms of efficiency, for extreme off-design operating conditions.

The increase of uncertainty when the performance prediction model is used in these operating conditions is mainly due to the nature of the experimental data-set from which the model has been derived: indeed, at low flow rates, a high dispersion of the efficiency data is shown; this affects the accuracy of the proposed model as already stated in [18]. For this reason, it is suggested to use this prediction model in the range ±40% of flow rates with respect to the BEP one. Furthermore, far from the BEP, the number of experimental data is also low. An improvement of the proposed model for extremely low flow rate values can be achieved if another non-dimensional parameter, which is always related to the knowledge of the BEP, is inserted in both Eq.s (11) and (12).

5.3. Analysis of the PaT flow field

Since the hydraulic machine investigated in this study was designed to operate exclusively in pump mode, the flow conditions in turbine mode encounter several adverse geometrical aspects such as: i) large width of the volute, ii) sharp edges of PaT LEs and iii) unfavourable blade angles. In order to describe in detail the PaT performance in turbine mode and explain why the PaT BEP is different to the pump mode, the flow conditions at the volute-impeller interface and at the impeller-discharge pipe interface were investigated. Figure 9a shows the velocity triangles at the volute-impeller interface. The flow angle at the volute outlet α_v is estimated from the velocity triangle between the circumferential component of the absolute velocity v_u and the meridional velocity v_m, according to Eq. (15).

$$\alpha_v = \mathrm{atan}\frac{v_m}{v_u} \tag{15}$$

For this reason, the averaged (both in time and circumferentially) velocities v_u and v_m at the volute outlet are extracted from the CFD simulations pointing out that the flow angle at the volute outlet is $\alpha_v = 12°$. Consequently, the flow angle at the impeller inlet is estimated from the known blade geometry, i.e. from the blade angle β of the PaT LE. Specifically, β is equal to 31.6° and 36.3° at the impeller hub and shroud, respectively, thus achieving an average value of 34°. Considering the flow rate Q and the volute-impeller interface area $A_{vi} = \pi Db$, where D is the impeller outer diameter and b the width of the volute outlet, the meridional velocity v_m, without considering the blades encumbrance, is evaluated as $v_m = Q/A_{vi}$. The angular velocity u is calculated from the known impeller revolutions n as $u = \pi Dn$. Then, considering an infinite blade count and an average blade angle $\beta = 34°$, the circumferential component of the absolute velocity $v_{u\infty}$ and the required flow angle $\alpha_{i\infty}$ at the impeller inlet are known by the means of Eq.s (16) and (17) respectively.

$$v_{u\infty} = u - \frac{v_m}{\tan\beta} \tag{16}$$

$$\alpha_{i\infty} = \mathrm{atan}\frac{v_m}{v_{u\infty}} \tag{17}$$

Since the impeller has a finite number of blades, which is usually lower in pumps than in turbines, the flow tends to detach from the blade direction due to the pressure difference between suction and pressure sides of the blade channels, leading to a flow angle α_i that ensures a shock-free inlet different to $\alpha_{i\infty}$. There is a wide range of empirical formulas that allow to calculate this type of flow deviation [50, 51, 52, 53, 54, 55]. For instance, Gulich [32] introduces the so-called slip factor γ to calculate the circumferential component of the absolute velocity v_u for a finite number of blades.

$$\gamma = 0.98\left(1 - \frac{\sqrt{\sin\beta}}{z^{0.7}}\right)k_w \tag{18}$$

where k_w stands for the influence of the impeller inlet diameter, which corresponds to the discharge diameter when the PaT operates in turbine mode, calculated using the formula reported in [32], while z is the number of blades. Then, the difference between $v_{u\infty}$ and v_u is calculated as follows:

$$v_{u\infty} - v_u = (1-\gamma)\,u_2 \tag{19}$$

Figure 9b shows the velocity triangle at the impeller inlet of the PaT. The flow angle α_i, given from this velocity triangle, is necessary for the shock-free inflow. Thus, if the flow angle of the volute α_v is smaller or larger than the flow angle α_i derived by the impeller velocity triangle, flow separation and strong swirling flows might develop inside the impeller.

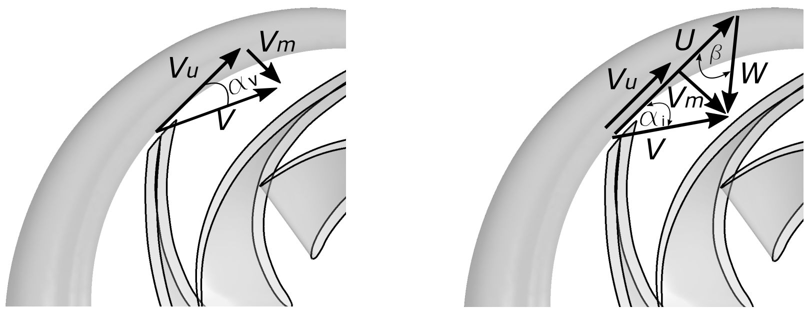

(a) Volute outlet (b) Impeller inlet

Figure 9: Description of the PaT velocity triangles at the volute-impeller interface

The flow angle at the volute outlet α_{vo} and the flow angle required for the shock-free impeller inflow α_i are listed in Table 13 considering the simulated flow rates Q. It must be noticed that, for the estimation of α_i, both the influence of blades encumbrance, thus the increase of v_m due to decrease of flow area, and slip factor are taken into account. Both α_i for a finite and $\alpha_{i\infty}$ for an infinite number

Table 13: Comparison between the PaT flow angles α at the volute-impeller interface

Flow rate Q [m^3/s]	φ	α_{vo} [°]	α_i [°] ($\alpha_{i\infty}$ [°])
0.0261	.0163	12.0	7.4 (6.6)
0.0312	0.0195	12.0	9.2 (8.0)
0.0360	0.0225	12.0	10.9 (9.5)
0.0391	**0.0244**	**12.0**	**12.2** (10.5)
0.0409	0.0255	12.0	12.9 (11.1)
0.0415	0.0259	12.0	13.1 (11.3)

of blades are shown. On the other hand, the flow angle at the volute outlet α_{vo}, given by the volute geometry, remains constant; the flow angle required for the shock-free inflow becomes larger when the flow rate Q increases, leading to a higher meridian velocity v_m. The results show that the ideal flow conditions are reached at flow rate around $Q = 0.0391$ m^3/s where the α_i is almost equal to α_{vo}. Beside the flow angle α, the circumferential component of the absolute velocity v_u is estimated at the volute outlet and at the impeller inlet. The difference between the v_u values at the volute outlet and at the impeller inlet per each analyzed flow rate Q, respectively, is shown in Table 14. The flow fields

Table 14: Comparison between the PaT v_u difference at the volute-impeller interface

Flow rate Q	φ	v_u @volute outlet	v_u @impeller inlet	difference
0.0261 m^3/s	0.0163	10.42 m/s	17.07 m/s	−6.65 m/s
0.0312 m^3/s	0.0195	12.46 m/s	16.42 m/s	−3.96 m/s
0.0360 m^3/s	0.0225	14.37 m/s	15.81 m/s	−1.44 m/s
0.0391 m^3/s	**0.0244**	**15.61** m/s	**15.41** m/s	+**0.2** m/s
0.0409 m^3/s	0.0255	16.33 m/s	15.18 m/s	+1.15 m/s
0.0415 m^3/s	0.0259	16.57 m/s	15.10 m/s	+1.47 m/s

obtained in the volute and in the impeller with the various analysed flow rates are shown in Figure 10. While at flow rate range $Q = 0.0360 - 0.409$ m^3/s a smooth flow inside the impeller is achieved, the secondary flow starts to appear with decreasing flow rates (see $Q = 0.0261$ m^3/s). From the results listed in Tables 13 and 14 and from flow fields shown in Figure 10, it is evident that the best inflow condition for the PaT impeller is achieved with a flow rate of about $Q = 0.0391$ m^3/s. This value is 4.4% lower than the BEP flow rate obtained from both the CFD analysis and measurements. Nevertheless, this evaluation was applied only for the flow conditions at the PaT impeller inlet, regardless the ones at the PaT impeller outlet. For this purpose, similarly as it was performed at the impeller inlet, the analytic analysis based on the velocity triangles might be applied also for the PaT impeller outlet as shown in Figure 11.

According to the PaT TE geometry of the blade angle, β is equal to 48.76° at the hub and 15.6° at the shroud, with an average value of 32.2°. Knowing the velocities u, v_m and the blade angle β, the other velocity components, v, v_u and w are then calculated.

The outlet blade angle of the hydraulic turbine runner is shaped so that the no-swirl or very low-swirl enters into the draft tube (discharge diffuser) at BEP conditions. This is ensured when the magnitude of the circumferential component related to the absolute velocity v_u is close to zero. This condition is important in order to avoid possible formation of vortex ropes since helical vortex structures cause high pressure fluctuations and stresses on the mechanical parts of the machine [36, 56, 57, 58, 59]. In a case of a pump that operates in turbine mode, the flow exiting from the impeller usually enters into a simple discharge pipe having a constant diameter, instead of a diffuser-like draft tube. This is the case of the investigated PaT where the flow exiting from the impeller is influenced only by the abrupt cross-sectional change due to the end of the hub geometry.

Consequently, beside the smooth flow inside the impeller, the convenient flow in the discharge pipe is suitable for the best PaT performance. From the Euler turbomachinery equations, the PaT head H_T is calculated according to Eq. (20), where the index 1 stands for the PaT impeller inlet, while index

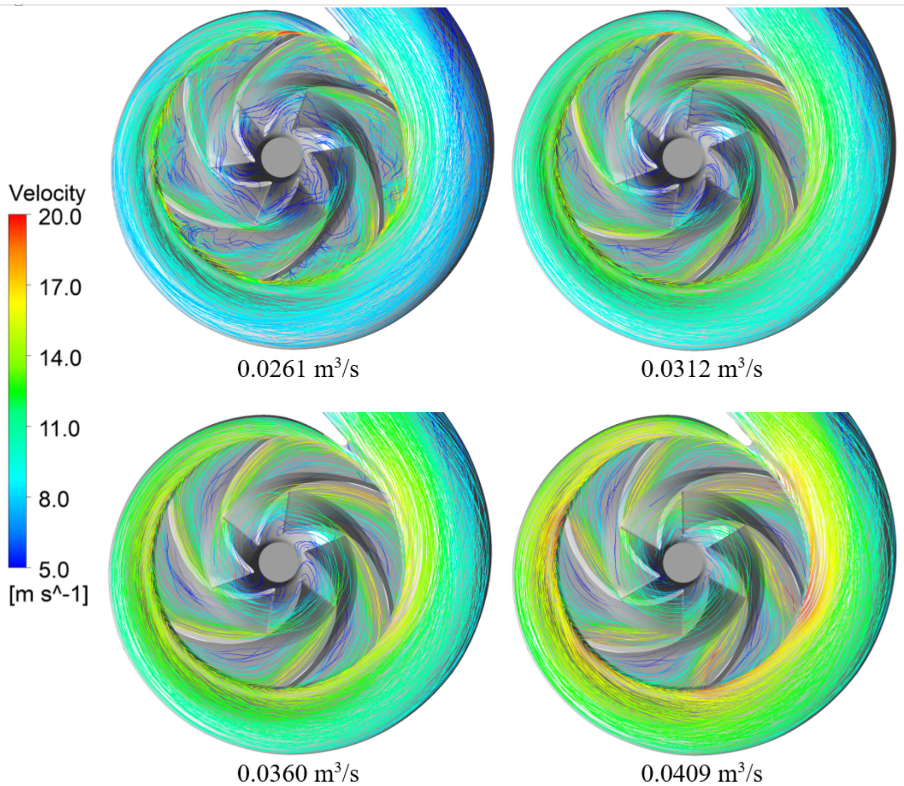

Figure 10: Volute-impeller streamlines at different flow rates

2 for the PaT impeller discharge. Since u_1 and u_2 are always positive, it is obvious that the co-rotating swirl (i.e. v_{u2} is positive) at the impeller discharge decreases H_T and, on the other hand, the counter-rotating swirl (i.e. v_{u2} is negative) increases H_T. The product $u_2 v_{u2}$ should have a minimal magnitude close to PaT BEP, while it becomes larger with decreasing or increasing Q.

$$H_T = \frac{u_1 v_{u1} - u_2 v_{u2}}{g \eta_h} \tag{20}$$

In order to asses this swirl amount exiting the PaT impeller, the magnitude of v_u at the impeller discharge is calculated according to Eq. (16), which is based on the outlet velocity triangle (see Figure 11) at three radial locations: hub, mid-span (50% of the span) and shroud.

The results are listed in Table 15 for various flow rates Q. Considering the 50% of the span, the minimal magnitude of v_{u2} is achieved for highest tested flow rate $Q = 0.0415$ m^3/s. Nevertheless, the large difference in v_{u2} between the hub and the shroud is noticeable due to the large variation of the blade angle β and the angular velocity u_2.

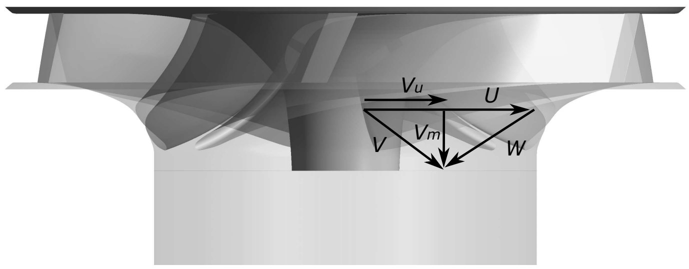

Figure 11: PaT velocity triangle at the impeller discharge

Table 15: Magnitude of the v_u component at the PaT discharge considering an infinite blade count

Flow rate Q	φ	$v_{u\infty}$ @hub	$v_{u\infty}$ @50% of the span	$v_{u\infty}$ @shroud
0.0261 m^3/s	0.0163	2.78 m/s	4.67 m/s	3.57 m/s
0.0312 m^3/s	0.0195	2.21 m/s	3.62 m/s	1.29 m/s
0.0360 m^3/s	0.0225	1.69 m/s	2.63 m/s	−0.85 m/s
0.0391 m^3/s	0.0244	1.35 m/s	1.99 m/s	−2.24 m/s
0.0409 m^3/s	0.0255	1.15 m/s	1.61 m/s	−3.05 m/s
0.0415 m^3/s	0.0259	1.09 m/s	1.49 m/s	−3.31 m/s

The analytic estimation of the $v_{u\infty}$ component from the velocity triangles, assuming an infinite blade count without a possible deviation of the relative velocity from the direction led by the blade angle β, is further compared with the v_u component extracted from the CFD results. For this purpose, a surface that is aligned with the PaT TE is constructed as shown in Figure 12 and the average value of v_u over this surface is calculated. The results are listed in Table 16 with the analytically estimated $v_{u\infty}$ component as an average value of $v_{u\infty}$ at the hub and $v_{u\infty}$ at the shroud. One can see that the smallest difference between analytic estimation and CFD results is found at flow rates around the BEP conditions, i.e. $Q = 0.0360 - 0.0415$ m^3/s, with decreasing magnitude towards the higher flow rate.

Chapallaz et al. [60] noticed that the effect of the circulation loss for a pump operating in turbine mode is practically negligible since it occurs at the inner periphery of the smaller impeller diameter d. Therefore, the slip factor for the PaT discharge is generally considered to be $\gamma = 1$ [61, 48]. Nonetheless, contrary to the low specific speed Francis turbine runners with relatively large number of blades (e.g. 15), the impellers of the radial pumps have a much smaller blade count, e.g. 6 in our case. As shown by Shi et al. [62] and Capurso et al. [63] the slip factor must be taken into account for estimation of turbine or PaT performance.

Figure 12: Surface generated for the extraction of the v_θ @PaT discharge

Table 16: Comparison of the v_u component between analytic and CFD results @PaT outlet

Flow rate Q	φ	$v_{u\infty}$ analytic	v_u CFD (surf. of rev.)	difference
0.0261 m^3/s	0.0163	5.26 m/s	6.93 m/s	−1.67 m/s
0.0312 m^3/s	0.0195	4.24 m/s	5.69 m/s	−1.45 m/s
0.0360 m^3/s	0.0225	3.29 m/s	4.12 m/s	−0.83 m/s
0.0391 m^3/s	0.0244	2.67 m/s	3.56 m/s	−0.89 m/s
0.0409 m^3/s	0.0255	2.32 m/s	3.049 m/s	−0.73 m/s
0.0415 m^3/s	**0.0259**	**2.20** m/s	**2.85** m/s	−**0.64** m/s

For this reason, the influence of a finite number of blades might be expected in our case, as proved by the velocity differences shown in Table 16, especially at lower flow rate; in these operating conditions, the secondary flows in the PaT impeller appear together with large circumferential components of the absolute velocity v_u.

Both analytically estimated and simulated values of v_u pointed out that the low swirling flow in the discharge pipe (v_u is close to zero) would be achieved at higher flow than the one corresponding to the PaT BEP. Considering Eq. (20) related to the estimation of the PaT head, it might be assumed that the co-rotating swirl (i.e. positive v_u) and its large magnitude is in agreement with a steep efficiency loss when the PaT operates at part-load conditions.

Figure 13 displays the streamlines at PaT discharge at four different flow rates $Q = 0.0261$ m^3/s, 0.0312 m^3/s, 0.0360 m^3/s and 0.0409 m^3/s, respectively. It can be noticed how the swirl condition in the PaT discharge pipes evolves, being an indicator of the performance of the machine in reverse mode.

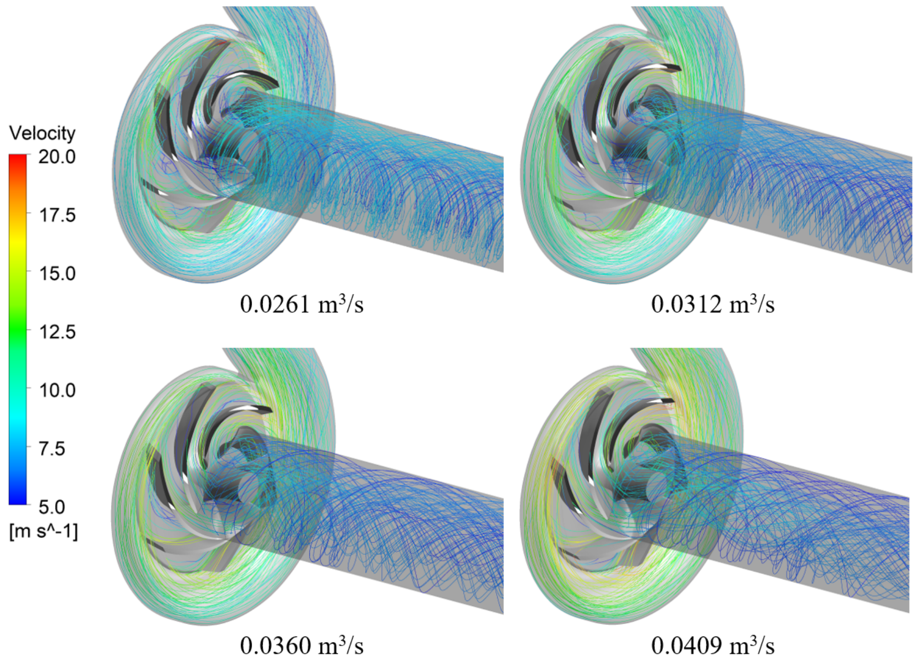

Figure 13: Comparison of the PaT flow fields in terms of streamlines

6. Conclusions

In this work, the behaviour of a Pump-as-turbine (PaT), exclusively designed to operate as a pump, is investigated experimentally in both pump and turbine operating modes; the machine fluid dynamic behaviour was also studied with numerical codes in turbine mode operation.

Laboratory tests were performed by means of a test rig that allows to test the PaT in both running modes - direct (pump mode) and reverse (turbine mode). Results showed an increase of the flow rate in turbine mode $Q_{BEP_{TURBINE}} = 1.27 \cdot Q_{BEP_{PUMP}}$ at the BEP, compared to the one in pump mode; this behaviour is in accordance with literature. Also the delivered head at the BEP $H_{BEP_{TURBINE}} = 1.41 \cdot H_{BEP_{PUMP}}$ increased in turbine mode, while the efficiency was slightly lower $\eta_{BEP_{TURBINE}} = 0.96 \cdot \eta_{BEP_{PUMP}}$.

CFD simulations of the PaT operating in turbine mode were carried out by using the same flow rates employed in the laboratory tests and validated through the experimental results. The values of the efficiency were corrected through the methodology presented in Section 3.1 due to the absence of impeller clearance. The results showed a good prediction accuracy of the PaT performance in correspondence of the BEP, where a maximum absolute relative error of 3.86% was detected for the evaluation of the mechanical efficiency, and at flow rates close to the rated one. Higher relative errors were obtained at extremely part-load operating condition, at a flow rate that is almost -60% with respect to the BEP one, because even a small error could result in a very high relative difference.

As an additional term of comparison, the analytical PaT performance prediction model developed by Rossi et al. [18] was briefly described and used. Weighting up the experimental values with the predicted ones, a maximum absolute relative percentage error of about 14% was obtained for the evaluation of the efficiency for a flow rate coefficient equal to 0.0163, while it worked well close to the BEP. The increase of uncertainty when the prediction model is used in extremely off-design operating conditions is due to the uncertainty of the behaviour of PaTs at part-load conditions: flow detachment phenomena and swirling flows can occur depending on the specific design and size of the machine. For this reason, it is suggested to use the model mainly in a range of flow rates that varies within $\pm 40\%$ of the Q_{BEP_T} to avoid the effect of the data dispersion.

A detailed study of the velocity triangles of the PaT operating in turbine mode allowed to carry out an insight of the fluid flow behaviour at the impeller inlet and outlet. This analysis was based on both analytic calculations and on the analysis of the CFD simulations. The analytic results showed good prediction of BEP flow rate with only small (5%) deviation from experiment and CFD. There could be two possible explanations: i) the real flow angle is influenced by the finite number of blades resulting in flow deviation and secondary flow, and ii) the PaT LE has a sharp end (no-rounded) since the PaT is designed to operate only in pump mode which might be responsible for flow separation. The PaT efficiency curve presents a consistent drop when dealing with very low part-load operating conditions. The reason of this behaviour is probably due to the high swirling flow detected at the discharge pipe when the flow rate decreases. The swirling flow at the discharge pipe is mainly generated by the circumferential component of the absolute velocity v_u: in particular, the positive values of v_u and their large magnitudes due to the rotating swirling flow might be the reason of a steep efficiency trend when the PaT operates at part-load conditions.

After the evaluation of the flow field by the means of the CFD simulations, a further step would be the implementation of some design solutions, as cheap and easy as possible, to facilitate the realignment of the flow at the the discharge pipe at part-load conditions. This would limit the efficiency drop detected during the experimental and numerical results.

Acknowledgments

This work has been carried out within the Research project "AI-ALPEN", CUP: B26J16000300003 funded by the Autonomous Province of Bozen/Bolzano - Italy for University Research-2014.

The EFRE-FESR project "TURB_HYDRO, Hydrokinetic turbines, optimization for sustainable production" (ERDF 2018-2021, CUP: I56C18000040009) support is also acknowledged.

Research has been supported by the project "Computer Simulations for Effective Low-Emission Energy Engineering" funded as project No. CZ.02.1.01/0.0/0.0/16_026/0008392 by Operational Programme Research, Development and Education, Priority axis 1: Strengthening capacity for high-quality research and project of Ministry of Education, Youth and Sports of the Czech Republic LTARF18019.

Acronyms

3D	Three-dimensional
BC	Boundary condition
BEP	Best Efficiency Point
CFD	Computational Fluid Dynamics
DES	Detached Eddy Simulations
FI	Flow Indicator
G	Electric Generator
G1	Fine grid
G2	Medium grid
G3	Coarse grid
GCI	Grid Convergence Index
LE	Leading Edge
LI	Level Indicator
M	Electric Motor
OP	Operating Point
PaT	Pump-as-Turbine
PFD	Process Flow Diagram
PI	Pressure indicator
RANS	Reynolds Averaged Navier-Stokes
RMS	Root Mean Square
TE	Trailing Edge
TI	Temperature Indicator
URANS	Unsteady Reynolds Averaged Navier-Stokes
WDN	Water Distribution Network

610 **Greek symbols**

α	Flow angle [°]
β	Blade angle [°]
γ	Slip factor [-]
Δ	Difference [-]
ϵ	Dissipation of turbulent kinetic energy [m^2/s^2]
η	Efficiency [-]
κ	Turbulent kinetic energy [m^2/s^2]
μ	Dynamic viscosity [Pa/s]
ν	Kinematic viscosity [St]
π	Pi [-]
ρ	Density [kg/m^3]
φ	Flow coefficient [-]
ψ	Head coefficient [-]
ω	Rotational speed [rad/s]

Nomenclature

a	Generic variable [-]
A	Area [m^2]
b	Volute outlet width [m]
D	Impeller diameter [m]
g	Gravitational acceleration [m/s^2]
H	Delivered head [m]
I	Turbulent intensity [-]
k_w	Influence of the impeller inlet diameter (pump mode)
N	Total number of grid elements [-]
P	Mechanical power [W]
Q	Volumetric flow rate [m^3/s]
r	Grid refinement factor [-]
t	Time [s]
T	Mechanical torque [Nm]
u	Angular velocity [m/s]
v	Absolute velocity [m/s]
V	Element's volume [m^3]
w	Relative velocity [m/s]
y	Distance normal to the surface
z	Number of impeller blades [-]

Subscripts

$*$	Dimensionless variables
∞	Infinite blade count
1	One
2	Two
3	Three
a	Generic variable
d	Disk friction
CFD	Computational Fluid Dynamics
$Exp.$	Experiment
ext	Extrapolated
h	Hydraulic
i	Impeller
m	Meridional component
$mod.$	Performance prediction model
m	Mechanical
n	Normalized quantity
P	Pump mode
s	Specific speed
T	Turbine mode
u	Circumferential component
v	Volumetric
vo	Volute
vi	Volute-Impeller interface

Superscripts

$*$	Dimensionless variables
$+$	Dimensionless variables in turbulent flows near a boundary
p	Apparent order of the method

References

[1] F. Pugliese, F. D. Paola, N. Fontana, M. Giugni, G. Marini, Experimental characterization of two Pumps As Turbines for hydropower generation, Renewable Energy 99 (2016) 180–187. `doi:10.1016/j.renene.2016.06.051`.

[2] M. Kramer, K. Terheiden, S. Wieprecht, Pumps as turbines for efficient energy recovery in water supply networks, Renewable Energy 122 (2018) 17–25. `doi:10.1016/j.renene.2018.01.053`.

[3] G. M. Lima, E. Luvizotto, B. M. Brentan, Selection and location of Pumps as Turbines substituting pressure reducing valves, Renewable Energy 109 (2017) 392–405. doi:10.1016/j.renene.2017.03.056.

[4] V. S. Jain, R. N. Patel, Investigations on pump running in turbine mode: A review of the state-of-the-art, Renewable and Sustainable Energy Reviews 30 (2014) 841–868. doi:10.1016/j.rser.2013.11.030.

[5] A. A. Williams, Pumps as turbines for low cost micro hydro power, Renewable Energy 9 (1996) 1227–1234. doi:10.1016/0960-1481(96)88498-9.

[6] M. Arriaga, Pump as turbine – A pico-hydro alternative in Lao People's Democratic Republic, Renewable Energy 35 (2010) 1109–1115. doi:10.1016/j.renene.2009.08.022.

[7] K. Sharma, Small Hydroelectric Project-Use of Centrifugal Pumps as Turbines, Tech. rep., Kirloskar, Electric Co., Bangalore, India (1985).

[8] A. A. Williams, The Turbine Performance of Centrifugal Pumps: A Comparison of Prediction Methods, Proceedings of the Institution of Mechanical Engineers, Part A: Journal of Power and Energy 208 (1994) 59–66. doi:10.1243/PIME_PROC_1994_208_009_02.

[9] C. Alatorre-Frenk, Cost minimisation in micro-hydro systems using Pump as Turbine, Ph.D. thesis, University of Warwick (1994).

[10] X. Tan, A. Engeda, Performance of centrifugal pumps running in reverse as turbine: Part II- systematic specific speed and specific diameter based performance prediction, Renewable Energy 99 (2016) 188–197. doi:10.1016/j.renene.2016.06.052.

[11] M. Liu, L. Tan, S. Cao, Theoretical model of energy performance prediction and bep determination for centrifugal pump as turbine, Energy 172 (2019) 712–732. doi:10.1016/j.energy.2019.01.162.

[12] S. Barbarelli, M. Amelio, G. Florio, Predictive model estimating the performances of centrifugal pumps used as turbines, Energy 107 (2016) 103–121. doi:10.1016/j.energy.2016.03.122.

[13] S. S. Yang, S. Derakhshan, F. Y. Kong, Theoretical, numerical and experimental prediction of pump as turbine performance, Renewable Energy 48 (2012) 507–513. doi:10.1016/j.renene.2012.06.002.

[14] S. Huang, G. Qiu, X. Su, J. Chen, W. Zou, Performance prediction of a centrifugal pump as turbine using rotor-volute matching principle, Renewable Energy 108 (2017) 64–71. doi:10.1016/j.renene.2017.02.045.

[15] D. Novara, A. McNabola, A model for the extrapolation of the characteristic curves of pumps as turbines from a datum best efficiency point, Energy Conversion and Management 174 (2018) 1–7. doi:10.1016/j.enconman.2018.07.091.

[16] J. Delgado, L. Andolfatto, D. I. C. Covas, F. Avellan, Hill chart modelling using the hermite polynomial chaos expansion for the performance prediction of pumps running as turbines, Energy Conversion and Management 187 (2019) 578–592. doi:10.1016/j.enconman.2019.02.051.

[17] M. Venturini, L. Manservigi, S. Alvisi, S. Simani, Development of a physics-based model to predict the performance of pumps as turbines, Applied Energy 1231 (2018) 343–354. doi:10.1016/j.apenergy.2018.09.054.

[18] M. Rossi, M. Renzi, Analytical Prediction Models for Evaluating Pumps-as-Turbines (PaTs) Performance, Energy Procedia 118 (2017) 238–242. doi:10.1016/j.egypro.2017.07.011.

[19] T. Wang, F. Kong, B. Xi, Y. Bai, C. Wang, The method for determining blade inlet angle of special impeller using in turbine mode of centrifugal pump as turbine, Renewable Energy 109 (2017) 518–528. doi:10.1016/j.renene.2017.03.054.

[20] S. S. Yang, F. Y. Kong, W. M. Jiang, X. Y. Qu, Effects of impeller trimming influencing pump as turbine, Computer & Fluids 67 (2012) 72–78. doi:10.1016/j.compfluid.2012.07.009.

[21] M. Binama, W. T. Su, W. H. Cai, X. B. Li, A. Muhirwa, B. Li, E. Bisengimana, Blade trailing edge position influencing pump as turbine (PAT) pressure field under part-load conditions, Renewable Energy 136 (2019) 33–47. doi:10.1016/j.renene.2018.12.077.

[22] H. J. Choi, M. A. Zullah, H. W. Roh, P. S. Ha, S. Y. Oh, Y. H. Lee, CFD validation of performance improvement of a 500 kW Francis turbine, Renewable Energy 54 (2013) 111–123. doi:10.1016/j.renene.2012.08.049.

[23] R. Tao, X. Zhou, B. Xu, Z. Wang, Numerical investigation of the flow regime and cavitation in the vanes of reversible pump-turbine during pump mode's starting up, Renewable Energy 141 (2019) 9–19. doi:10.1016/j.renene.2019.03.108.

[24] A. Maleki, M. M. Ghorani, M. H. S. Haghighi, A. Riasi, Numerical study on the effect of viscosity on a multistage pump running in reverse mode, Renewable Energy 150 (2020) 234–254. doi:10.1016/j.renene.2019.12.113.

[25] Y. Liu, L. Tan, Tip clearance on pressure fluctuation intensity and vortex characteristic of a mixed flow pump as turbine at pump mode, Renewable Energy 129 (2018) 606–615. doi:doi.org/10.1016/j.renene.2018.06.032.

[26] M. Rossi, G. Comodi, N. Piacente, M. Renzi, Effects of viscosity on the performance of Hydraulic Power Recovery Turbines (HPRTs) by the means

of Computational Fluid Dynamics (CFD) simulations, Energy Procedia 148 (2018) 170–177. doi:10.1016/j.egypro.2018.08.046.

[27] J. González, J. M. F. Oro, K. M. A. Díaz, C. Santolaria, Flow analysis for a double suction centrifugal machine in the pump and turbine operation modes, International Journal for Numerical Methods in Fluids 61 (2008) 220–236. doi:10.1002/fld.1951.

[28] C. S. Morros, J. M. F. Oro, K. M. A. Díaz, Numerical modelling and flow analysis of a centrifugal pump running as a turbine: Unsteady flow structures and its effects on the global performance, International Journal for Numerical Methods in Fluids 65 (2011) 542–562. doi:10.1002/fld.2201.

[29] X. Su, S. Huang, X. Zhang, S. Yang, Numerical research on unsteady flow rate characteristics of pump as turbine, Renewable Energy 94 (2016) 488–495. doi:10.1016/j.renene.2016.03.092.

[30] J. Yang, G. Pavesi, X. Liu, T. Xie, J. Liu, Unsteady flow characteristics regarding hump instability in the first stage of a multistage pump-turbine in pump mode, Renewable Energy 127 (2018) 377–385. doi:10.1016/j.renene.2018.04.069.

[31] R. Barrio, J. Fernández, E. Blanco, J. Parrondo, A. Marcos, Performance characteristics and internal flow patterns in a reverse-running pump–turbine, SAGE journals 226 (2011) 695–708. doi:10.1177/0954406211416304.

[32] J. F. Gülich, Centrifugal Pumps, 3, Springer-Verlag Berlin Heidelberg, 2014. doi:10.1007/978-3-642-40114-5.

[33] P. J. Roache, K. N. Ghia, F. M. White, Editorial Policy Statement on the Control of Numerical Accuracy, Journal of Fluids Engineering 108. doi:10.1115/1.3242537.

[34] P. J. Roache, Conservatism of the GCI in Finite Volume Computations on Steady State Fluid Flow and Heat Transfer, Journal of Fluids Engineering 125. doi:10.1115/1.1588692.

[35] I. B. Celik, U. Ghia, P. J. Roache, C. J. Freitas, H. Coleman, P. E. Raad, Editorial Policy Statement on the Control of Numerical Accuracy, Journal of Fluids Engineering 108. doi:10.1115/1.2960953.

[36] G. D. Ciocan, M. S. Iliescu, T. C. Vu, B. Nennemann, F. Avellan, Experimental study and numerical simulation of the FLINDT draft tube rotating vortex, J. Fluids Eng 129 (2) (2007) 146–158.

[37] D. Jošt, A. Škerlavaj, M. Morgut, P. Mežnar1, E. Nobile, Numerical simulation of flow in a high head Francis turbine with prediction of efficiency, rotor stator interaction and vortex structures in the draft tube, in: Journal

of Physics: Conference Series, Vol. 579, 2015. doi:10.1088/1742-6596/579/1/012006.

[38] P. Mössinger, R. Jester-Zürker, A. Jung, Investigation of different simulation approaches on a high-head Francis turbine and comparison with model test data: Francis-99, in: Journal of Physics: Conference Series, Vol. 579, 2015. doi:10.1088/1742-6596/579/1/012005.

[39] B. Mulu, An experimental and numerical investigation of a Kaplan turbine model, Ph.D. thesis, Lulea University of Technology, Luleå, Sweden (2012).

[40] D. Štefan, S. Houde, C. Deschênes, Numerical Investigation of Flow in a Runner of Low-Head Bulb Turbine and Correlation With Particle Image Velocimetry and Laser Doppler Velocimetry Measurements, J. Fluids Eng 141 (9) (2019) 18. doi:10.1115/1.4042963.

[41] R. R. Parchen, W. Steenberg, An Experimental and Numerical Study of Turbulent Swirling Pipe Flows, Journal of Fluids Engineering 120 (1) (1998) 54–61. doi:10.1115/1.2819661.

[42] O. Petit, A. I. Bosioc, H. Nilsson, S. Muntean, R. F. Susan-Resiga, Unsteady Simulations of the Flow in a Swirl Generator, Using OpenFOAM, International Journal of Fluid Machinery and Systems 4 (1) (2011) 199–208. doi:10.5293/IJFMS.2011.4.1.199.

[43] M. Ariff, S. M. Salim, S. C. Cheah, Wall y^+ approach for dealing with turbulent flow over a surface mounted cube: part 1 – low Reynolds number, in: Seventh International Conference on CFD in the Minerals and Process Industries, CSIRO, Australia, 2009.

[44] M. Ariff, S. M. Salim, S. C. Cheah, Wall y^+ approach for dealing with turbulent flow over a surface mounted cube: part 2 – high Reynolds number, in: Seventh International Conference on CFD in the Minerals and Process Industries, CSIRO, Australia, 2009.

[45] R. Izmaylov, H. Lopulalan, G. Norimana, Unsteady flow modeling using transient rotor-stator interface, ASME Turbo Expo 2013: Turbine Technical Conference and Exposition (2013) 8.

[46] ANSYS© software - 4.12.2 Standard Wall Functions.
URL http://www.afs.enea.it/project/neptunius/docs/fluent/html/th/node99.htm

[47] M. Rossi, A. Nigro, M. Renzi, Experimental and numerical assessment of a methodology for performance prediction of Pumps-as-Turbines (PaTs) operating in off-design conditions, Applied Energy 248 (2019) 555–566. doi:10.1016/j.apenergy.2019.04.123.

[48] A. Carravetta, S. Derakhshan, H. Ramos, Pump as Turbine - PAT, Springer, Cham, 2018. doi:10.1007/978-3-319-67507-7_2.

[49] M. Rossi, M. Righetti, M. Renzi, Pump-as-Turbine for Energy Recovery Applications: The Case Study of An Aqueduct, Energy Procedia 101 (2016) 1207–1214. doi:10.1016/j.egypro.2016.11.163.

[50] A. Stodola, Steam and gas turbines, P. Smith, New York, 1945.

[51] F. J. Wiesner, A Review of Slip Factors for Centrifugal Impellers, Journal of Engineering for Power 89 (4) (1966) 9. doi:10.1115/1.3616734.

[52] Z. Waisser, Vliv změny geometrických tvarů průtočné části odstředivých čerpadel na jejich parametry, Academia (1976) 139.

[53] K. S. Paeng, M. K. Chung, A new slip factor for centrifugal impellers, Proceedings of the Institution of Mechanical Engineers, Part A: Journal of Power and Energy 2015 (5) (2001) 645–649. doi:10.1243/0957650011538776.

[54] X. Qiu, D. Japikse, J. Zhao, M. R. Anderson, Analysis and Validation of a Unified Slip Factor Model for Impellers at Design and Off-Design Conditions, Journal of Turbomachinery 133 (4) (2011) 9. doi:10.1115/1.4003022.

[55] Y. L. Zhang, Z. C. Zhu, H. S. Dou, B. L. Cui, Y. Li, J. J. Xiao, A Method to Determine the Slip Factor of Centrifugal Pumps through Experiment, International Journal of Turbo & Jet-Enginesdoi:10.1515/tjj-2014-0014.

[56] R. S. Resiga, G. D. Ciocan, I. Anton, F. Avellan, Analysis of the Swirling Flow Downstream a Francis Turbine Runner, Journal of Fluids Engineering 128 (1) (2006) 177–189. doi:10.1115/1.2137341.

[57] M. S. Iliescu, G. D. Ciocan, F. Avellan, Analysis of the Cavitating Draft Tube Vortex in a Francis Turbine Using Particle Image Velocimetry Measurements in Two-Phase Flow, J. Fluids Eng 130 (2) (2008) 10. doi:10.1115/1.2813052.

[58] D. Štefan, P. Rudolf, Proper Orthogonal Decomposition of Pressure Fields in a Draft Tube Cone of the Francis (Tokke) Turbine Model, Journal of Physics: Conference Series 579 (1). doi:10.1088/1742-6596/579/1/012002.

[59] D. Štefan, P. Zubík, M. Hudec, P. Rudolf, Numerical and experimental investigation of swirling flow in a conical diffuser, EPJ Web of Conferences 92 (2015) 5. doi:10.1051/epjconf/20159202085.

[60] J. M. Chapallaz, P. Eichenberger, G. Fischer, Manual on Pumps used as Turbines, Vol. 11, Skat, 1992.

[61] S. S. Yang, S. Derakhshan, F. Y. Kong, Theoretical, numerical and experimental prediction of pump as turbine performance, Renewable Energy 48 (201) 507–513. doi:10.1016/j.renene.2012.06.002.

[62] G. Shi, X. Liu, J. Yang, S. Miao, J. Li, Theoretical research of hydraulic turbine performance based on slip factor within centripetal impeller, Advances in Mechanical Engineering 7 (7) (2015) 12. doi:10.1177/1687814015593864.

[63] T. Capurso, M. Stefanizzi, G. Pascazio, S. Ranaldo, S. Camporeale, B. Fortunato, M. Torresi, Slip Factor Correction in 1-D Performance Prediction Model for PaTs, Water 11 (565) (2019) 23. doi:10.3390/w11030565.